Mohsen, A., Kind, R., Yuan, X. (2020): Seismic discontinuities in the lithospheric mantle at the dead sea transform. - Geophysical Journal International, 223, 3, 1948-1955.

https://doi.org/10.1093/gji/ggaa430

Geophysical Journal International

Geophys. J. Int. (2020) **223,** 1948–1955
Advance Access publication 2020 September 12
GJI Seismology

doi: 10.1093/gji/ggaa430

Seismic discontinuities in the lithospheric mantle at the Dead Sea Transform

Ayman Mohsen,[1] Rainer Kind[2,3] and Xiaohui Yuan[2]

[1]*Department of Geography, Faculty of Economics and Social Studies, An-Najah National University, Nablus, Palestine*
[2]*GeoForschungsZentrum GFZ,* 14473 *Potsdam, Germany. E-mail: kind@gfz-potsdam.de*
[3]*Freie Universität, Fachrichtung Geophysik,* 12249 *Berlin, Germany*

Accepted 2020 September 4. Received 2020 September 3; in original form 2020 March 16

SUMMARY

The Dead Sea Transform (DST) was formed in the mid-Cenozoic, about 18 Myr ago, as a result of the breakaway of the Arabian plate from the African plate. Higher resolution information about the sub-Moho structure is still sparse in this region. Here, we study seismic discontinuities in the mantle lithosphere in the region of the DST using a modified version of the *P*- and *S*-receiver function methods. We use open data from permanent and temporary seismic stations. The results are displayed in a number of depth profiles through the study area. The Moho is observed on both sides of the transform at nearly 40 km depth by *S*-to-*p* and in *P*-to-*s* converted signals. The lithosphere–asthenosphere boundary (LAB) on the eastern side of the DST is observed near 180–200 km depth, which is according to our knowledge the first LAB observation at that depth in this region. This observation could lead to the conclusion that the thickness of the Arabian lithosphere east of the DST is likely cratonic. In addition, we observe in the entire area a negative velocity gradient at 60–80 km depth, which was previously interpreted as LAB.

Key words: Body waves; Continental margins: transform; Dynamics of lithosphere and mantle.

1 INTRODUCTION

Our study area is located at the Dead Sea Transform (DST, see Fig. 1), which is a major left lateral strike-slip fault that accommodates the relative motion between the Arabian and African plates (Garfunkel *et al.* 1981; LePichon & Gaulier 1988). The DST was formed roughly 18 Myr ago as a result of the mid-Cenozoic breakaway of the Arabian plate from the African plate, which until then were parts of a continuous continent (Garfunkel & Ben-Avraham 1996). It extends for more than 1000 km and moves with a slip rate of roughly 0.5 cm yr^{-1} (El-Isa 1990; Girdler 1990; Klinger *et al.* 2000). Faccenna *et al.* (2013) suggested that large-scale mantle flow from the Afar Plume is responsible for tectonic processes in the entire eastern Mediterranean area. This could include thinning of the Arabian lithosphere at its eastern edge due to rifting of the Red Sea (e.g. Hansen *et al.* 2007). Hansen *et al.* (2007) observed lithospheric thinning from the centre of Arabia towards the Red Sea using *S*-receiver functions. Here, we study the thickness of the lithosphere in the DST area using a modified version of the receiver function technique.

The thickness of the lithosphere in the entire DST region is poorly constrained by previous seismic studies (Mohsen *et al.* 2006), yet several geophysical studies have been conducted in different subregions with methods such as reflection/refraction profiles (Makris *et al.* 1983; El-Isa *et al.* 1987a,b; DESERT Group 2004; Mechie *et al.* 2005), local source tomography (Koulakov & Sobolev 2006), gravity (Al-Zoubi & Ben-Avraham 2002; Goetze *et al.* 2006) and teleseismic studies (Hofstetter & Bock 2004; Mohsen *et al.* 2005, 2011). These previous geophysical studies have provided information about the thickness of the crust in different parts of the study area. In addition, a lower crustal discontinuity was observed only on the eastern part of the transform, at a depth of 30 km (DESERT Group 2004; Mechie *et al.* 2005; Mohsen *et al.* 2005; Goetze *et al.* 2006).

Considering the lithospheric mantle, Ginzburg *et al.* (1979, 1981) have reported a mantle reflected *P* phase at a depth of 55 km along a refraction profile extending from the southernmost part of the Gulf of Aqaba to the Dead Sea Basin. El-Isa (1990) noted from traveltime modelling of local earthquakes an upper-mantle refractor at 55 km depth with a gradual velocity reduction underneath station UNJ in Jordan. Hofstetter & Bock (2004) have reported a velocity decrease at about 60–70 km beneath the EIL and JER stations of the Israel seismic network from *P*-receiver functions. Mohsen *et al.* (2006, 2013) have reported from *S*-receiver functions a discontinuity at 65–80 km depth east of the DST which was interpreted as the lithosphere–asthenosphere boundary (LAB). Mohsen *et al.* (2006), however, report no LAB observations near 100 km depth at station RAYN on the central part of the Arabian shield. Instead they observe

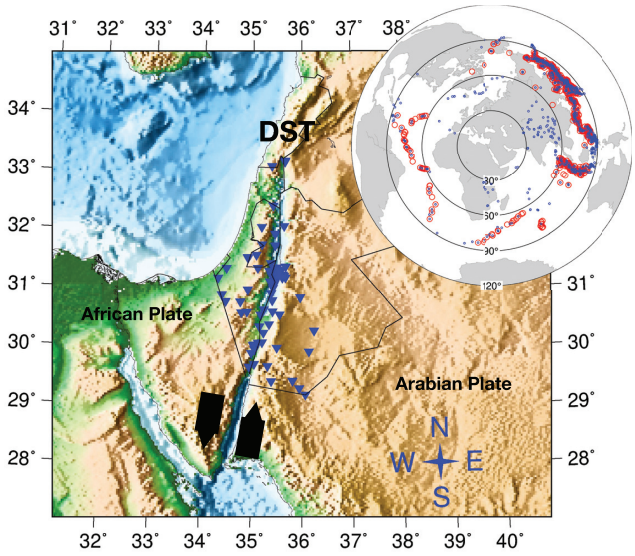

Figure 1. Station locations in the study area (inverted triangles). Blue dots in the inset mark the epicentres of the events used for the *Ps* conversions and red circles for the *Sp* conversions, respectively.

at that station a velocity reduction near 160 km depth, which could be interpreted as a typical LAB depth for a cratonic region. Kumar *et al.* (2007) confirmed this observation with receiver function data. Blanchette *et al.* (2018) report a lithospheric thickness of about 60 km at the western boundary of the Arabian craton at the Red Sea. Hansen *et al.* (2007) report an increase of the lithospheric thickness from about 50–160 km from the western edge of the Arabian craton to its centre using *S*-receiver functions. Tang *et al.* (2019) used data from the Saudi National Seismic Network for a joint interpretation of *P*- and *S*-receiver functions and surface waves. They found a low velocity zone between 70 and 190 km depth beneath western Arabia. Similar results had been obtained by Al-Amri (2015) from practically the same database. Laske *et al.* (2008) did not observe a low velocity zone in the upper-mantle east of the DST in a fundamental mode Rayleigh wave study. However, in more recent studies Kounoudis *et al.* (2020), Liu *et al.* (2020) and Schaeffer & Lebedev (2013) derived from traveltime and waveform tomography models with low velocities at 100–200 km depth on both sides of the DST. The purpose of this paper is to obtain a more detailed image of the upper-mantle discontinuities near the DST using *S*-to-*p* and *P*-to-*s* converted waves from a larger amount of data than has previously been used.

2 DATA AND METHOD

We used broad-band data from the Israel National Seismic Network (network code IS), GEOFON stations in the DST region (network code GE) and from the temporary networks DESIRE (network code Z4) and DESERT (network code ZR). All stations are open to the public. The locations of the stations used are shown in Fig. 1. The data have been obtained from the GEOFON archive of the GeoForschungsZentrum GFZ Potsdam. Seismic signals have been downloaded from teleseismic earthquakes with magnitudes greater than 5.5 at epicentral distances between 60° and 85° for *SV* signals, and from 40° to 85° for *P* signals. The distribution of the teleseismic earthquake sources is shown in Fig. 1. Most epicentres are concentrated in the northeastern backazimuth quadrant.

Converted seismic waves have been used since about the 1970s to study the structure of the upper mantle. Jordan & Frazer (1975) and Faber & Müller (1980) picked arrival times of converted waves in analogue records and obtained the depth of the corresponding discontinuity from the time difference with respect to the main phase generating the conversion. Only a few large earthquakes produced converted waves which were strong enough so that they could be detected in single records. Since many digital records are now available, many converted waves may be stacked to raise the converted signals above the noise level. Langston (1979) introduced deconvolution in the receiver function technique for source equalization before stacking. In this method, the reference times are determined from the maximum amplitudes of the deconvolved signals. We went back to the traditional method and picked the arrival times of the parent phases (on the *SV* component in the case of *Sp* conversions and on the *P* component for *Ps* conversions) as reference time. A distance moveout correction is usually applied if traces are summed in time domain. For time to depth transformation back projection along the ray path within the global IASP91 model (Kennett & Engdahl 1991) is used here. Profiles across the study area are computed with this method. The original broad-band data are used. No filter is applied to avoid possible problems with sidelobes.

The first processing step is to rotate the original components Z, N, E into the L, Q, T (or *P*, *SV*, *SH*) system. We used the theoretical backazimuth and angle of incidence determined from the global IASP91 reference model. The first arrivals of the *SV* and *P* signals were automatically picked using the algorithm of Baer & Kradolfer (1987). The traces have been normalized with respect to the absolute maximum within the time window of 10 s around the *S* or *P* onset on the *SV* or *P* component, respectively. As the expected converted wave amplitudes are between 1 per cent and 10 per cent of the incident signal, we only use records with amplitudes of the converted phases less than 30 per cent of the incident wave. While this may permit some signals which are much larger than expected, this is a key trade-off between maximizing data count and limiting noisy traces. After applying these procedures, we obtained 2966 useful *Sp* and about 3500 useful *Ps* records from 86 stations. To process the data, we used the seismic handler package (Stammler 1993, www.seismic-handler.org).

3 RESULTS OF SEISMOLOGICAL OBSERVATIONS

In Figs 2 and 3, we have summed all depth migrated *Sp* (Figs 2a and 3a) and *Ps* (Figs 2b and 3b) data in two profiles which are oriented perpendicular and along the DST. In contrast to the common receiver functions, the depth of the converted waves must be determined from the onset of the converted signals and not from the maximum amplitudes as in deconvolved traces. Zero depth marks the onset times of the *P* or *SV* signals. The onset of the converted signals in the *Sp* profiles is at the lower end of the converted signal and in the *Ps* profiles at the top end of the converted signal. This is because in *Sp* traces the conversions are precursors of the *SV* phase and in *Ps* traces the conversions are in the coda of the *P* phase. The *Ps* images are mirrored at the Earth's surface in order to obtain figures comparable with the *Sp* images. We have indicated several phases using dashed lines as the Moho, NVG (negative velocity gradient) and LAB. Many of these phases can be followed over several hundred kilometres and will be discussed later. The NVG and LAB are negative signals produced by a velocity reduction with depth, whereas the Moho is a positive signal, indicating velocity increase

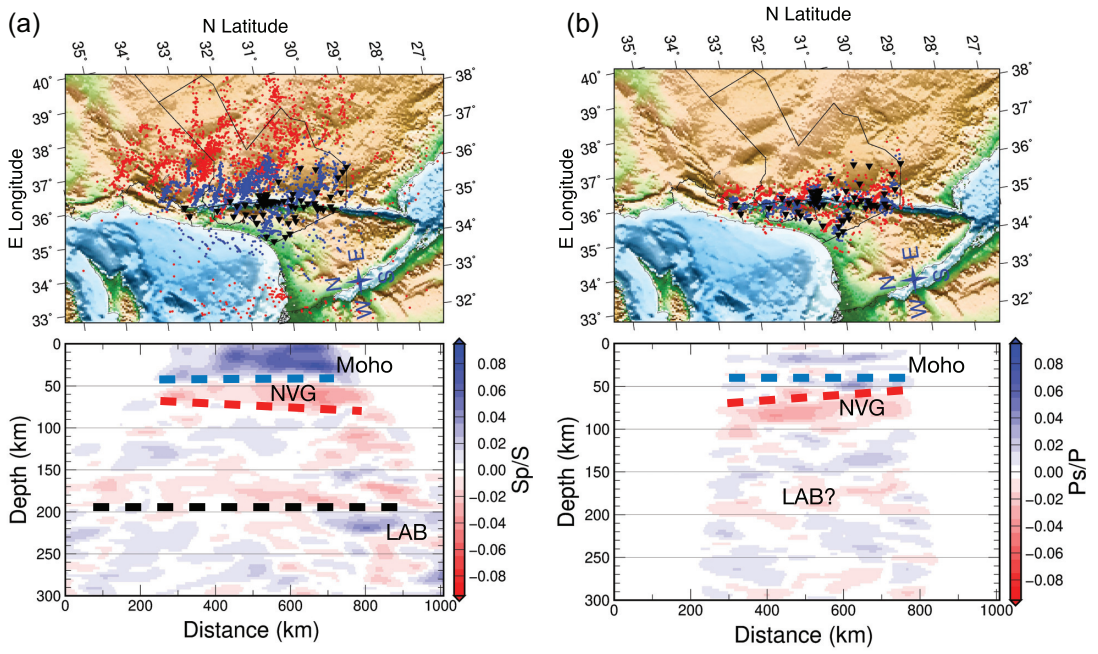

Figure 2. Depth migrated north–south profiles of (a) *Sp* and (b) *Ps* conversions at the DST using all available data. Red and blue dots in the maps indicate theoretical piercing points at 180 and 70 km depth, respectively. Blue colours in the data indicate seismic discontinuities with velocity increase downward. Red colours indicate velocity decreases downward. 'Moho' marks the crust-mantle boundary, 'NVG' a negative velocity gradient zone and 'LAB' the lithosphere–asthenosphere boundary. Conversions are marked by continuous lines at the beginning of the signal and not at the centre as in the traditional receiver functions.

with depth. The scatter or noise in the data is clearly larger to the west of the DST than the east as a consequence of sparser data coverage from the west.

In Figs 4 and 5, two north–south profiles parallel to the DST are shown, covering only the area east or west of it. In Figs 6 and 7, two east–west profiles are shown covering the area in the northern and southern parts of the DST. The width of the profiles is marked by the two black lines in the maps. All signals travelling between these two lines are included in the stacking.

3.1 Lithosphere–asthenosphere boundary

In the *Sp* conversions east of the DST (Figs 2a–4a, 6a and 7a), we observe at 180–200 km depth a negative signal coherent laterally over many hundreds of kilometres, indicating a velocity reduction marked LAB.

In the Figs 2(b)–4(b) and 7(b), we see in the *Ps* conversions in the same depth range also a negative signal marked LAB too. However, since the *Ps* conversions arrive in the coda of the *P* waves where also various multiples arrive, these multiples might mask the conversions from the LAB. For that reason we have added a question mark at the LAB label. There is no obvious LAB signal observed on the western side of the DST in both the *Sp* and *Ps* data (Fig. 5, see also Supporting Information). We note that only 237 of the total 2966 *Sp* traces used have piercing points at 200 km depth on the west side of the DST. This is a consequence of the locations of the epicentres of most events used, which are in the northeastern quadrant of the backazimuths. To our knowledge the LAB has not been observed before at 180–200 km depth so close to the DST. Mohsen *et al.* (2006) report from *S*-receiver functions a LAB depth decreasing from 80 km north of the Dead Sea to about 67 km at the Gulf of Aqaba. We also observe in our *Sp* data a discontinuity at the same depths, which we interpret as NVG zone but not as the LAB. Mohsen *et al.* (2006, 2013) did not observe the deeper LAB which we observe here. This is probably due to the sparser data at these earlier times. Hansen *et al.* (2007) also report a depth of less than 80 km for the LAB in Jordan, near the Gulf of Aqaba and along the Red Sea from *S*-receiver functions. They found the largest LAB depth in the Arabian plate to be almost 160 km at station RAYN in the centre of the plate, confirming the result of Mohsen *et al.* (2006). Tang *et al.* (2019), report a low velocity zone between 70 and 190 km in western Arabia. Al-Amri (2015) indicates a velocity reduction below RAYN at 60 km depth, but not near 160 km. Blanchette *et al.* (2018) also found a similarly shallow LAB at about 60 km near the Red Sea coast. Al-Amri (2015) observed the LAB at 80 km depth near the Gulf of Aqaba. This is just south of the stations we are using. However, the piercing points at 180 km depth of the rays recorded at our stations reach to the northern end of the Gulf of Aqaba (see Fig. 7a). Our observations of a LAB depth typical for a craton east of the DST may be, however, in agreement with the surface wave observations of Laske *et al.* (2008), who did not observe an upper-mantle low velocity zone east of the DST. In Fig. 8 is shown in time domain the summation trace of all *Sp* records east of 36° longitude. The conversions at the Moho, the NVG and the LAB are marked. The LAB signal arriving about 20 s before the *SV* main phase is clearly above the noise level. In Fig. 9 are shown

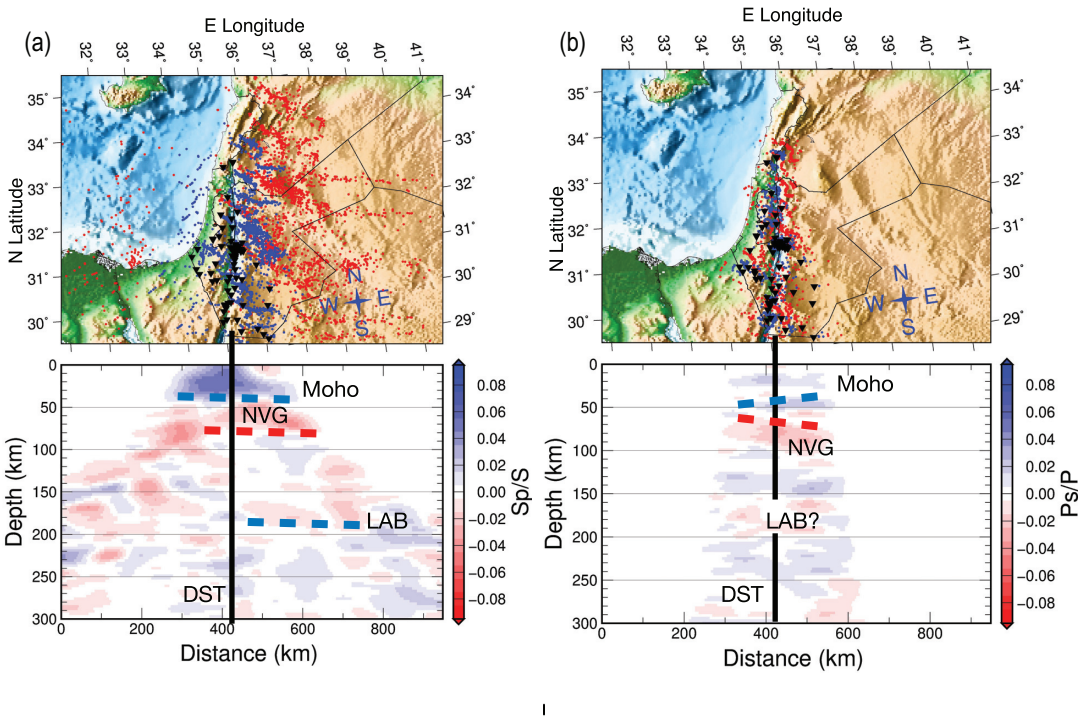

Figure 3. Same as Fig. 2, but for an east–west profile. The vertical line in the profile marks the location of the DST.

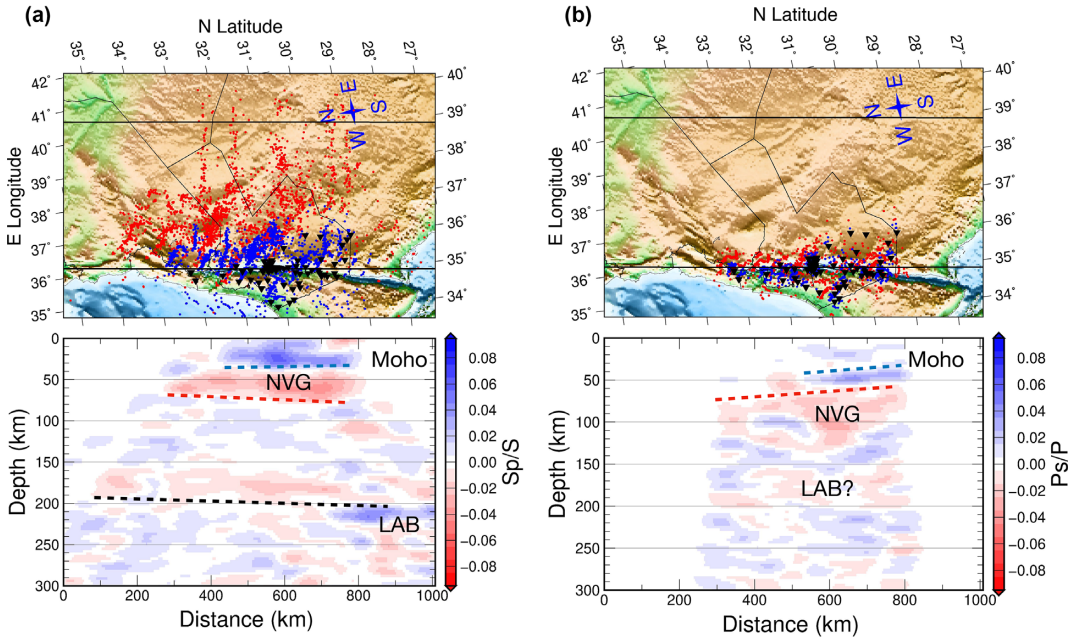

Figure 4. Same as Fig. 2, but using data only on the east side of the DST. The two black lines mark the width of the profile. All traces within this region are summed.

summation traces of the station EIL at the northern tip of the Gulf of Aqaba which also show the LAB clearly. This figure also illustrates that the summation trace is below the noise level of the individual records. The craton-like structure at the DST is probably difficult to reconcile with the suggestions of far northward material flow from the Afar plume (see e.g. Faccenna *et al.* 2013).

3.2 Negative velocity gradient at 50–100 km depth

There are clear observations of negative signals (marked NVG) between 50 and 100 km depth in all *Ps* and *Sp* profiles in Figs 2–7. Although these phases are in approximately the same depth range, there are in some cases large differences between the *Sp* and the *Ps* results. For example in the north–south profiles (Figs 2 and 4)

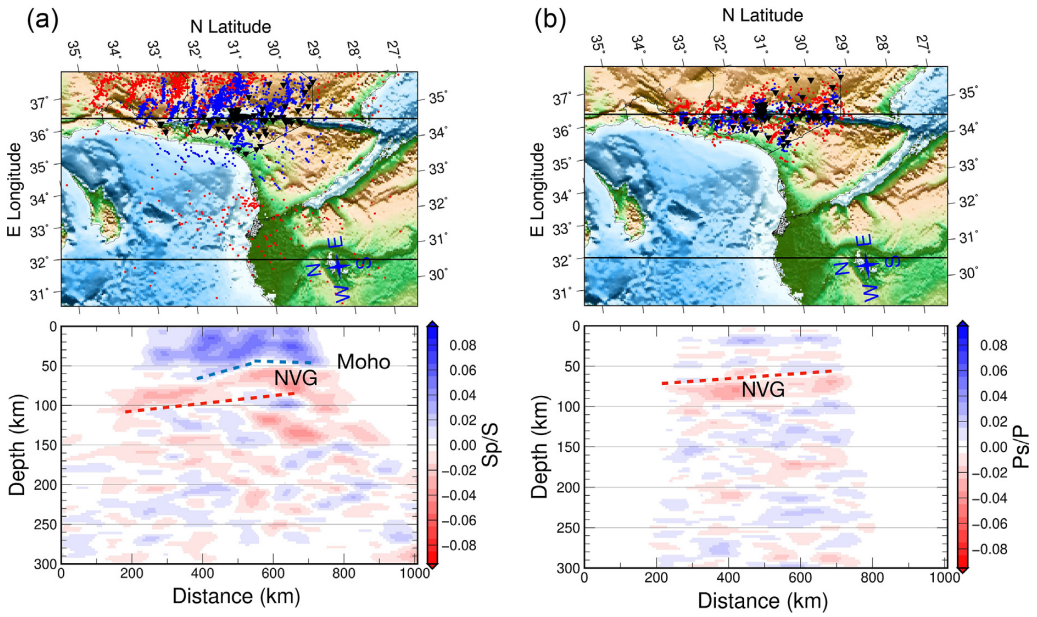

Figure 5. The same images as in Fig. 4, but for the west of the DST.

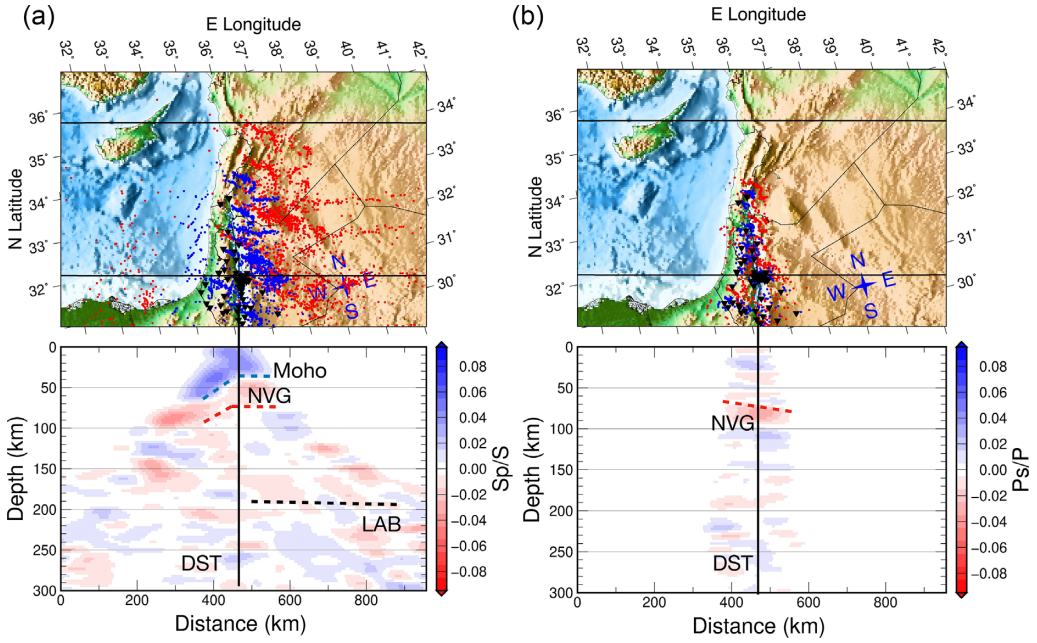

Figure 6. East–west (a) *Sp* and (b) *Ps* profiles in the northern part of the study area. Moho, NVG and LAB are observable only on the eastern side of the DST. There are fewer rays (piercing points) west of the DST which leads to very unclear images there.

they dip in opposite directions. The *Ps* data are north dipping and the *Sp* data south dipping. Using fewer *S*-receiver functions but of high quality, Mohsen *et al.* (2006) identified the LAB dipping from 67 km depth in the south to 80 km in the north. This is very similar to our *Ps* observations of the NVG east and west of the DST. Our *Sp* observations west of the DST (Fig. 5) indicate a similar dip of the NVG but at a 20–30 km larger depth. On all east–west profiles (Figs 3, 6 and 7) the NVG appears nearly horizontal in the *Sp* data and is dipping towards the east in the *Ps* data. There exist a number of possible reasons for the discrepancy between some of the *Sp* and *Ps* data. The first reason is that the piercing points of both methods are at very different locations (see distribution of piercing points). The *Sp* piercing are up to150 km away from the stations whereas the Ps piercing points are only a few tens of kilometres away. These piercing points are computed for a laterally homogeneous model (IASP91). In case of lateral heterogeneity this could make a big difference. The incidence angles of the *Sp* and *Ps* conversions are very different and act therefore differently to heterogeneity. A second reason may be that in the *Ps* data multiples in the crustal interior could modify the direct conversions from the NVG (see e.g. Mohsen *et al.* 2005). The *Sp* conversion are practically free of such multiples. The LAB in the *Sp* data does not indicate a dipping structure. The possible LAB signal in the *Ps* data also does not have a significant dip. This confirms that our migration method, which was derived for horizontal layering is indeed working for horizontally layered structures, but might

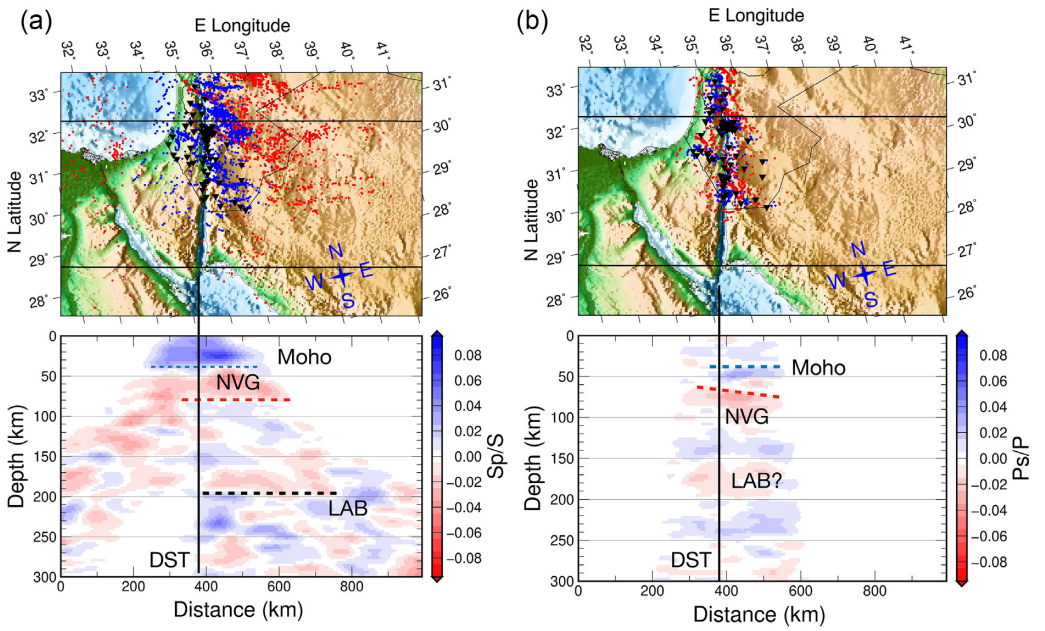

Figure 7. Same as in Fig. 6, but for the southern part of the study area. Here too, the information west of the DST seems much less certain, although the Moho seems unchanged across the DST.

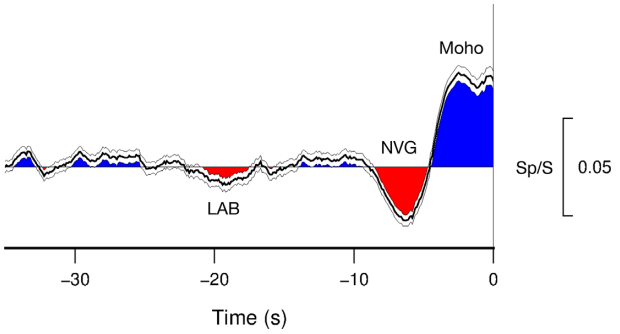

Figure 8. Distance moveout corrected and summed traces with piercing points at 180 km depth east of 36° longitude. The LAB signal is well above the $\pm 2\sigma$ error bounds of the bootstrap mean.

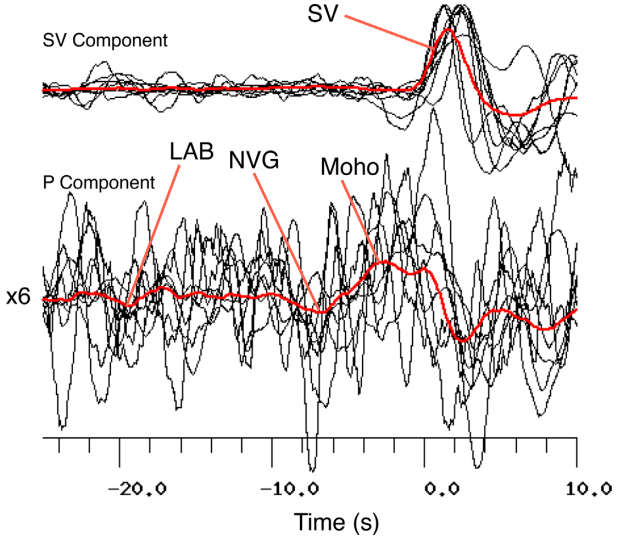

Figure 9. Seismic traces of station EIL (Eilat) which is located in southernmost Israel at the tip of the Gulf of Aqaba. Red lines are the summations of all 498 traces used from this station. Black lines are 9 arbitrarily selected individual records. Amplitudes of the *P* component traces are enlarged by a factor of 6.

have problems for strongly inclined discontinuities. We think higher resolution data coverage and migration methods for heterogeneous structures could help to solve the problem. However, since the NVG is not the main target of this paper we shift the comparison of *Sp* and *Ps* data in case of lateral heterogeneity to a later time.

Hansen *et al.* (2007) observed a similar discontinuity like our NVG zone close to the DST, which they interpreted as LAB. No comparable signal at a similar depth is observed at station RAYN in the central part of the Arabian plate. However there are many observations of NVG zones in several cratons which are interpreted as the mid-lithospheric discontinuity (MLD) caused by slow velocity minerals or fabric changes due to deformation (see e.g. Aulbach *et al.* 2017). For example, Hopper and Fischer (2015) and Krueger *et al.* (2019) studied the MLD below the North American craton. Kind *et al.* (2020) also studied the MLD in the same region with the same technique applied here. A conclusion of these studies is that the MLD is a very elusive structure there. Our conclusion for the area east of the DST is that because the depth at which the LAB is expected in cratons is near 200 km, the structure interpreted as the LAB by Mohsen *et al.* (2006) might be the MLD.

3.3 Moho

Sp conversion at the Moho are in all figures stronger than in the *Ps* data. In Figs 5 and 6, for example, *Ps* conversions at the Moho are practically missing, although they are strong in the *Sp* data. These data may even indicate north and west dipping of the Moho to the west of the DST. However, due to the data sparseness there, we consider this uncertain. We also note that in Fig. 5, the NVG is in *Sp* and *Ps* data also dipping towards the north. The converted signal from the Moho is clear in the *Sp* conversions in Figs 4 and 7, whereas it is in the *Ps* data less clear but visible. In Fig. 4, the Moho deepens from 30 km in the south to 40 km in the north to the east of the DST. Fig. 7 shows clearly that the Moho is observed at

about 40 km depth in both *Sp* and *Ps* data in the southern part of the study area across the DST. The Moho in the entire region west of the DST looks relatively heterogeneous in the *Sp* data (Fig. 5a). Also, the *Ps* conversions in Fig. 5(b) (west of DST) show only some very unclear indications for the Moho. The same is true for the *Ps* Moho conversions in Fig. 6(b) (north-east quadrant). The Moho conversions in the *Sp* phases in Figs 5(a) and 6(a) look very complicated, similar to the NVG data in the corresponding figures. This might be an indication of strong lateral heterogeneity in the lithosphere below the Mediterranean. However, it could also be due to the sparseness of data from westerly directions. Since the Moho is also not the main goal of the present study we refrain from a more detailed discussion.

4 CONCLUSIONS

We applied a simplified version of the receiver function technique which avoids deconvolution and possible related artefacts. This new method has shown in this paper once more its usefulness. The main result is the observation of a negative (velocity decrease downward) seismic discontinuity at 180–200 km depth on the east side of the DST, which we interpret as LAB. These observations seem surprising compared with earlier observations reporting 60–80 km depth for the LAB there. We also observe an additional NVG at the same shallow depth. This means that we have observed two NVG zones in the uppermost mantle east of the DST. We interpreted the shallower one (at 60–80 km) as the MLD, which is observed in several other cratons. In the central part of the Arabian craton, at station RAYN, NVGs have been reported also at two different depths (at 60 and 160 km) by different authors. To resolve the significance of our new observations more data should be analysed from additional stations on the Arabian craton. Our observations would indicate that the original structure of the craton at the DST is relatively unchanged in geological history. This could lead to the conclusion that the opening of the Red Sea, which might have caused lithospheric thinning there, had relatively little influence on the lithospheric structure east of the DST. This was already indicated by surface wave observations of Laske *et al.* (2008). In summary, to the east of the DST, the lithospheric structure is relatively unmodified craton with MLD and deep LAB intact. However, west of the DST, data are too sparse to clearly identify the LAB.

ACKNOWLEDGEMENTS

This research was supported by the Deutsche Forschungsgemeinschaft. We would like to thank Jim Mechie for valuable suggestions and for reading the manuscript, and Robert Porritt and an anonymous reviewer for constructive reviews.

REFERENCES

Al-Amri, A.M., 2015. Lithospheric structure of the Arabian shield from joint inversion of P- and S-receiver functions and dispersion velocities, *Acta Geol. Pol.,* **65**(2), 229–245.

Al-Zoubi, A. & Ben-Avraham, Z., 2002. Structure of the Earth's crust in Jordan from potential field data, *Tectonophysics,* **346,** 45–59.

Aulbach, S., Massuyeau, M. & Gaillard, F., 2017. Origins of cratonic mantle discontinuities: a view from petrology, geochemistry and geodynamic models, *Lithos,* **268-271,** 364–382.

Baer, M. & Kradolfer, U., 1987. An automatic phase picker for local and teleseismic events, *Bull. seism. Soc. Am.,* **77**(4), 1437–1445.

Blanchette, A.R., Klemperer, S.L., Mooney, W.D. & Zahran, H.M., 2018. Two- stage Red Sea rifting inferred from mantle earthquakes in Neoproterozoic lithosphere, *Earth. Planet. Sci. Lett.,* **497,** 92–101.

DESERT Group., 2004. The crustal structure of the Dead Sea transform, *Geophys, J. Int.,* **156,** 655–681.

El-Isa, Z.H., Mechie, J., Prodehl, C., Makris, J. & Khim, R., 1987a. A crustal structure study of Jordan derived from seismic refraction data, *Tectonophysics,* **138,** 235–253.

El-Isa, Z.H., Mechie, J. & Prodehl, C., 1987b. Shear velocity structure of Jordan from explosion seismic data, *Geophys. J. R. astr. Soc.,* **90,** 265–281.

El-Isa, Z.H., 1990. Lithospheric structure of the Jordan Dead Sea Transform from earthquakes data, *Tectonophysics,* **180,** 29–36.

Faber, S. & Müller, G., 1980. Sp phases from the transition zone between the upper and lower mantle, *Bull. seism. Soc. Am.,* **70,** 487–508.

Faccenna, C., Becker, T.W., Jolivet, L. & Keskin, M., 2013. Mantle convection in the Middle East: reconciling Afar upwelling, Arabia indentation and Aegean trench rollback, *Earth. Planet. Sci. Lett.,* **375,** 254–260.

Garfunkel, Z., Zak, I. & Freund, R., 1981. Active faulting along the Dead Sea Rift, in *The Dead Sea Rift,* Freund, R. & Garfunkel, Z., eds. Tectonophysics, Vol. **80,** pp. 1–26.

Garfunkel, Z. & Ben-Avraham, Z., 1996. The structure of the Dead Sea basin, *Tectonophysics,* **266,** 155–176.

Ginzburg, A., Makris, J., Fuchs, K., Prodehl, C., Kaminski, W. & Amitia, U., 1979. A seismic study of the crust and the upper mantle of the Jordan Dead sea rift and their transition toward the Mediterranean Sea, *J. geophys. Res.,* **84,** 1569–1582.

Ginzburg, A., Makris, J., Fuchs, K. & Prodehl, C., 1981. The structure of the crust and upper mantle in the Dead Sea rift. in Freund, R. & Garfunkel, Z., eds.,, The Dead Sea Rift, *Tectonophysics,* Vol. **80,** pp. 109–120

Girdler, R.W., 1990. The Dead Sea Transform fault system, *Tectonophysics,* Vol. **180,** pp. 1–13.

Goetze, H.J., El-Kelani, R., Schmidt, S., Rybakov, M., Foerster, H.J. & Ebbing, J., 2006. Integrated 3-D density modelling and segmentation of the Dead Sea Transform, *Int. J. Earth. Sci.,* **96**(2), 289–302.

Hansen, S.E., Rodgers, A.J. & Schwartz, S.Y., 2007. Imaging ruptured lithosphere beneath the Red Sea and Arabian Peninsula, *Earth. Planet. Sci. Lett.,* **259**(3–4), 256–265, https://escholarship.org/uc/item/4ps1684s.

Hofstetter, A. & Bock, G., 2004. Shear-wave velocity structure of the Sinai subplate from receiver function analysis, *Geophys. J. Int.,* **158,** 67–84.

Hopper, E. & Fischer, K.M., 2015. The meaning of midlithospheric discontinuities: a case study in the northern U.S. craton, *Geochem. Geophys. Geosyst.,* **16,** 4057–4083.

Jordan, T.H. & Frazer, L.N., 1975. Crustal and upper mantle structure from Sp phases, *J. geophys. Res.,* **80,** 1504–1518.

Kennett, B.L.N. & Engdahl, E.R., 1991, Travel times for global earthquake location and phase identification, *Geophys. J. Int.,* **105,** 429–465.

Kind, R., Mooney, W.D. & Yuan, X., 2020. New insights into structural elements of the upper mantle beneath the contiguous United States from S-to-P converted waves, *Geophys. J. Int.,* **222,** 646–659.

Klinger, Y., Avouac, J.P., Abou Karaki, N., Dorbath, L., Bourles, D. & Reyss, J.L., 2000. Slip rate on the Dead sea transform fault in northern Araba valley (Jordan), *Geophys. J. Int.,* **142,** 755–768.

Koulakov, I. & Sobolev, S., 2006. Moho depth and 3 D P and S structure of the crust and uppermost mantle in the Eastern Mediterranean and Middle East derived from tomographic inversion of local ISC data, *Geophys. J. Int.,* **164,** 218–235.

Kounoudis, R., Bastow, I.D., Ogden, C.S., Goes, S., Jenkins, J., Grant, B. & Braham, C., 2020. Seismic tomographic imaging of the Eastern Mediterranean mantle: implications for terminal-stage subduction, the uplift of Anatolia, and the development of the North Anatolian Fault, *Geochem. Geophys. Geosyst.,* **21**(7), https//doi.org/10.1029/2020GC009009.

Krueger, H.E., Fischer, K.M., Gama, I., Hua, J. & Eilon, Z., 2019. Do mid-Lithospheric Discontinuities exist? *AGU Fall Meeting,* San Francisco, abstract#T21A–03.

Kumar, P., Yuan, X.M., Kumar, R., Kind, R., Li, X. & Chadha, R.K., 2007. The rapid drift of the Indian tectonic plate, *Nature,* **449**(7164), 894–897.

Laske, G. & Weber, M., Desert Working Group, 2008. Lithospheric structure across the Dead Sea Transform as constrained by Rayleigh

waves observed during the DESERT experiment, *Geophys. J., Int.,* **173,** 593–610.
Langston, C.A., 1979. Structure under Mount Rainier, Washington, inferred from teleseismic body waves, *J. geophys. Res.,* **84,** 4749–4762.
LePichon, X. & Gaulier, J.M., 1988. The rotation of Arabia and the Levant fault system, *Tectonophysics,* **153,** 271–294.
Liu, L., Tong, S., Li, S. & Qaysi, S., 2020. Sp receiver-function images of African and Arabian lithosphere: survey of newly available broadband data, *Seismol. Res. Lett.,* **91,** 1813–1819.
Makris, J., Ben-Avraham, Z., Behle, A., Ginzburg, A., Giese, P., Steinmetz, L., Whitmarsch, R.B. & Eleftheriou, S., 1983. Seismic profiles between Cyprus and Israel and their interpretation, *Geophys. J. R. astr. Soc.,* **75,** 575–591.
Mechie, J., Abu-Ayyash, K., Ben-Avraham, Z., El-Kelani, R., Mohsen, A., Ruempker, G., Saul, J. & Weber, M., 2005. Crustal shear velocity structure across the Dead Sea Transform from 2-D modelling of project DESERT explosion seismic data, *Geophys. J., Int.,* **160,** 910–924.
Mohsen, A., Kind, R., Sobolev, S. & Weber, M., DESERT Group, 2006. Thickness of the lithosphere east of the Dead Sea Transform, *Geophys. J. Int.,* **167,** 845–852.
Mohsen, A., Hofstetter, R., Bock, G., Kind, R., Weber, M., Wylegalla, K. & Ruempker, G., DESERT Group, 2005. A receiver function study across the Dead Sea Transform, *Geophys. J. Int.,* **160,** 948–960.
Mohsen, A., Asch, G., Mechie, J., Kind, R., Hofstetter, R., Weber, M., Stiller, M. & Abu-Ayyash, K., 2011. Crustal structure of the Dead Sea Basin (DSB) from a receiver function analysis, *Geophys. J. Int.,* **184,** 463–476.
Mohsen, A., Asch, G., Kind, R., Mechie, J. & Weber, M., 2013. The lithosphere-asthenosphere boundary in the eastern part of the Dead Sea Basin (DSB) from S-to-P receiver functions, *Arab J. Geosci.,* **6,** 2343–2350.
Schaeffer, A.J. & Lebedev, S., 2013. Global shear speed structure of the upper mantle and transition zone, *Geophys. J. Int.,* **194,** 417–449.
Stammler, K., 1993. Seismic handler programmable multichannel data handler for interactive and automatic processing of seismological analysis, *Comput. Geosci.,* **19**(2), 135–140.
Tang, Z., Mai, P.M., Julià, J. & Zahran, H., 2019. Shear velocity structure beneath Saudi Arabia from the joint inversion of P and S wave receiver functions, and Rayleigh wave group velocity dispersion data, *J. geophys. Res.: Solid Earth,* **124,** 4767–4787.

SUPPORTING INFORMATION

Supplementary data are available at *GJI* online.

Figure S1. Map of study area. Blue inverted triangles are the stations and red dots are the piercing points at 200 km depth. Yellow dashed lines mark the profiles in the following Figs S2–S4.

Figure S2. (a) 150 km wide profile of migrated *S*-to-*p* converted phases (area between black lines). The LAB is clearly visible although the region covered by the profile is much smaller than the regions covered by the profiles in the main paper. (b) Same profile as in (a), however profile width is 100 km. (c) Same profile as in (a), however profile width is 50 km. The velocity reduction near 200 km depth (LAB) east of the DST remains a clearly visible signal also in narrower profiles. The detailed structure of the LAB, however, may change if fewer traces are available.

Figure S3. (a) Another profile in the study area. Profile width is 150 km. (b) Same profile as in Fig. 3(a), profile width is 100 km. (c) Same profile as in Fig. 3(a), profile width is 50 km. The LAB near 200 km depth is observed in both areas east of the DST covered by Figs S2 and S3.

Figure S4. A 100 km wide profile in the west of the DST. There exist few piercing points at 200 km depth within this profile and even less in the other areas west of the DST. No negative (red) signal is visible near 200 km depth. The reason for this could be that no LAB exists there, or there are too few data.

Please note: Oxford University Press is not responsible for the content or functionality of any supporting materials supplied by the authors. Any queries (other than missing material) should be directed to the corresponding author for the paper.